Eur. Phys. J. Special Topics **227**, 2559–2573 (2019)

https://doi.org/10.1140/epjst/e2019-800137-2

THE EUROPEAN PHYSICAL JOURNAL SPECIAL TOPICS

Regular Article

Electrokinetic Onsager coefficients and energy conversion in deformable nanofluidic channels

Mpumelelo Matse[1,a], Michael Eikerling[1,2], and Peter Berg[3]

[1] Department of Physics, Simon Fraser University, Burnaby, BC V5A 1S6, Canada
[2] Department of Chemistry, Simon Fraser University, Burnaby, BC V5A 1S6, Canada
[3] Department of Science, University of Alberta, Camrose, AB T4V 2R3, Canada

Received 27 August 2018 / Received in final form 3 November 2018
Published online 17 April 2019

Abstract. This work explores the nonlinear coupling between wall deformation and one-dimensional electrokinetic transport in a nanochannel with negatively charged walls. Within the framework of nonequilibrium thermodynamics, compact formulae are derived for the electrokinetic transport parameters in terms of Onsager phenomenological coefficients and, subsequently, for the energy conversion efficiency. Results confirm that Onsager's reciprocity principle holds for rigid channels. However, the methodology used to reduce to 1D does not maintain the symmetry of Onsager's matrix when the channel is deformed due to the introduction of a "fictitious" diffusion term of counter-ions. Furthermore, the model predicts a reduced efficiency of electrokinetic energy harvesting for channels with soft deformable walls.

1 Introduction

Electrokinetics is a complex field that is concerned predominantly with the coupled transport processes of ions and fluids in porous media. Nanoscale artificial and biological membranes that contain surface charges within their pores, have emerged as a major area in the study of fundamental transport mechanisms in electrokinetic fluid flows. The classical theory developed by Smoluchowski and Helmholtz [1,2] still remains the basis of continuum models [3–5] used to study electrokinetic systems. It rests on the concept of a diffuse electric double layer (EDL) – the exclusion of co-ions and the enrichment of counter-ions in a layer of fluid adjacent to the charged surface [6,7]. A practical need for a clear, fundamental understanding of the transport arises from the necessity to control and manipulate the flow rates for a wide array of engineering systems such as micro/nanofluidic devices [8], ion separation [9,10] and energy conversion devices [11,12].

In the framework of nonequilibrium thermodynamics, electrokinetic transport phenomena are observed as ions and fluid flow in response to thermodynamic driving forces. This approach to studying thermodynamically irreversible systems was formalized most prominently by Onsager in 1931 [13,14]. For electrochemical systems, prevalent thermodynamic forces are those prompted by drops in pressure or electrostatic potential, or by concentration gradients of ions. Onsager postulated that, near

[a] e-mail: mmatse@sfu.ca

equilibrium, fluxes are linear functions of conjugate thermodynamic forces. Hence, in the absence of concentration gradients, the coupled volumetric fluid flux and ion flux induced by pressure and electrostatic potential drops, are written in the following form,

$$\begin{pmatrix} \text{fluid} \\ \text{flux} \\ \\ \text{ion} \\ \text{flux} \end{pmatrix} = \begin{pmatrix} L_{11} & L_{12} \\ \\ L_{21} & L_{22} \end{pmatrix} \begin{pmatrix} \text{pressure} \\ \text{drop} \\ \\ \text{potential} \\ \text{drop} \end{pmatrix}, \tag{1}$$

where the L_{ij}'s are called the Onsager phenomenological transport coefficients. Here, L_{12} is proportional to the permeability of the porous medium, L_{11} corresponds to the effective electric conductivity, and L_{12} and L_{21} are the coefficients for the streaming current and the electroosmotic flow, respectively. Note that the above formulation assumes a vanishing concentration of co-ions, which is the case that this contribution focuses on.

Typically, an ion flux, driven by an electric field, generates a fluid flux and, conversely, a fluid flux, driven by a pressure drop, generates an ion flux. In equation (1), this coupling is reflected by the Onsager reciprocity principle, viz. $L_{12} = L_{21}$. This points to the use of electrokinetic effects for energy conversion. The two most widely studied effects can be described as follows: when an external electric field is imposed on an ion-fluid system, the electric force acts upon ions and, hence, exerts a volumetric force onto the entire fluid surrounding the ions, thereby dragging the fluid along (electroosmosis) [15]; likewise, under an applied hydrostatic pressure difference and in the absence of an external electric field, counter-ions that form the EDL are carried downstream with the fluid, equivalent to an electric streaming current that can either be counterbalanced or that will come to rest when a corresponding streaming potential is applied or has formed [16,17]. The first effect corresponds to an electrokinetic pumping mode, characterized by the conversion of electrical energy into mechanical energy. The second effect corresponds to a power generation mode, where electrical energy is harvested from kinetic energy of the fluidic system (see Fig. 1). For practical applications, one would like to maximize the efficiency of energy conversion processes in either system.

In this contribution, a deformable nanochannel, characteristic of proton-conducting cylindrical pores in polymer electrolyte membranes (PEMs), is considered. The most commonly used PEM material is Nafion, which consists of a polymeric elastic backbone, lined by grafted sidechains that are terminated with sulfonic acid head groups. Under hydrated conditions in a PEM, the acidic groups dissociate and release protons to the aqueous subphase [18,19]. Numerous studies have been undertaken toward a better understanding of hydration dynamics and transport phenomena in these membranes, motivated by the desire to understand deformation/swelling statics and dynamics for water sorption/desorption [20–22], dimensional stability of PEM [23,24], aging/crack formation [25,26], application in electroactuator devices [27–29] and transport of ions and solvent [30,31].

Closed-form formulae representing phenomenological coefficients are derived for the electrokinetic transport parameters and for the energy conversion efficiency. The work is based on the 1-D continuum mean-field model proposed by Matse et al. [32], which considers a water-filled deformable nanochannel with negatively charged and linearly elastic walls, balanced by counter-ions (only) inside the fluid. The mass and charge transport within this water-cation system is described by Poisson–Nernst–Planck–Stokes (PNP-Stokes) equations.

In essence, the study in this contribution is a special case of the more general analysis of co- and counter-ion flow inside charged nanochannels, conducted by

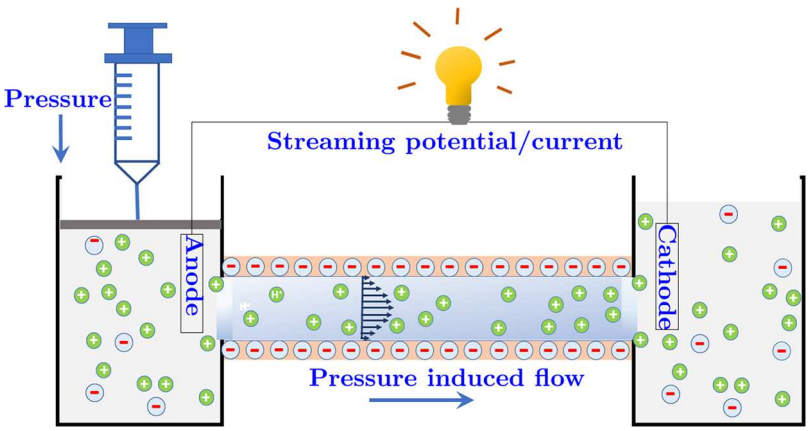

Fig. 1. Schematic illustration of electrokinetic power generation.

Peters et al. [33]. The difference is that the presence of co-ions considered in that work does not allow for the derivation of closed-form expressions and flow solutions but instead requires numerical calculations. The limiting case of counter-ions-only, on the other hand, neglects the crucial coupling of the channel to surrounding reservoirs via electric double layers at the channel ends which, among other things, determines the boundary conditions for the fluid flow in the channel interior.

The layout of the paper is as follows: Section 2 describes the model and presents the mathematical framework. Section 3 contains derivations and a discussion of the Onsager coefficients and the energy conversion efficiency of the electrokinetic system explored herein. Finally, Section 4 concludes this article with a summary and an outlook.

2 Model

2.1 Surface charges

Figure 1 shows a schematic diagram and the cross section of the deformable cylindrical nanochannel considered in this study. The channel is connected to two reservoirs and is characterized by an equilibrium radius R_0, wall thickness h_0 and length L_0. Inner walls of the cylindrical section are lined by negative charges with uniform surface charge density σ_0. Motivated by the PEM pore model [11], we take the polymeric pore walls to be comprised of dissociated anionic moieties exposed to an aqueous phase. The most commonly used material in PEMs is Nafion, which consists of a tetrafluoroethylene backbone and perfluoroalkyl ether side chains terminated in sulfonic acid groups that leave behind fixed anionic charges on the walls upon proton dissociation [18]. We assume that only hydrated proton-complexes (cations) and water are transported in the channels. Thermodynamic forces due to pressure and/or electrostatic potential gradients result in a dynamic displacement of water and protons, and induce the deformation of channel walls, represented by the resultant channel radius $R(z)$. Deformations propagate along the channel, creating gradients in proton concentration and electric field in axial direction.

The surface charge density at the channel walls is described by an empirical scaling law [21,22],

$$\sigma_s = \sigma_0 \times \left(\frac{R_0}{R}\right)^{\alpha}, \tag{2}$$

where the channel geometry parameter α measures the extent of surface group reorganization upon deformation, to mimic the physical properties of different nanoprotonic systems. For channels that decrease in length during swelling, $0 < \alpha \leq 1$ is satisfied. Weak surface charge reorganization corresponds to $\alpha \to 0$, whereas $\alpha \to 1$ indicates strong reorganization of surface charges. All along, it is assumed that the acid terminated side chains remain fully dissociated and that the total charge along the channel wall remains constant.

2.2 Fluid flow

The Stokes equations represent the conservation of fluid momentum in the channel and are used to calculate the fluid velocity $\mathbf{v} = [u_r(r,t), u_z(r,t)]^T$. These are given as

$$\nu\nabla^2\mathbf{v} - \nabla p + qc\mathbf{E} = 0, \tag{3}$$

along with the fluid continuity equation

$$\frac{\partial\rho}{\partial t} + \nabla\cdot(\rho\mathbf{v}) = 0. \tag{4}$$

Here, ρ is the fluid mass density, p the fluid pressure, ν the fluid dynamic viscosity, q the elementary charge, c the proton concentration, and $\mathbf{E} = [E_r(\mathbf{r},t), E_z(\mathbf{r},t)]^{\mathrm{T}}$ the electric field.

For high-aspect-ratio channels, $R_0 \ll L_0$, the rate of fluid flow is much slower in radial direction than in axial direction. Under this so-called lubrication approximation, flow is nearly one-dimensional. Using cross-sectional averaging and the lubrication approximation, as developed in reference [32], the 1-D Stokes equation (3) for the axial direction was found to be

$$\frac{8\nu}{R^2}\bar{u}_z + \frac{\partial\bar{p}}{\partial z} - q\bar{c}\bar{E}_z(1-\xi_u) = 0. \tag{5}$$

In this convention, $\bar{u}_z$, $\bar{p}$, $\bar{c}$, $\bar{E}_z$ represent cross-sectionally averaged values of the axial fluid velocity, fluid pressure, proton concentration and axial electric field, respectively. The function ξ_u can be expressed as the expansion,

$$\xi_u = \sum_{i=1}^{\infty}\frac{2\Lambda^i}{(i+1)(i+2)} = \frac{1}{3}\Lambda + \frac{1}{6}\Lambda^2 + \frac{1}{10}\Lambda^3 + \mathcal{O}(\Lambda^4). \tag{6}$$

Here, ξ_u is related to the flow solutions found by Berg et al. [4] for the case of an infinite, straight channel with a circular cross-section.

The parameter Λ, dimensionless and satisfying $0 \leq \Lambda < 1$ (and $0 \leq \xi_u < 1$), measures how strongly protons interact electrostatically and can be expressed in terms of the radial Debye length $\ell_D = \sqrt{\epsilon\epsilon_0 k_{\mathrm{B}}T/q^2 c_{r=0}}$, i.e., the distance from the charged wall over which electrostatic effects between wall charge and ions in the

solution persist, and the Bjerrum length $\ell_B = q^2/4\epsilon\epsilon_0 k_B T$, i.e., the distance at which the interaction between two unit charges equals their thermal energy $k_B T$:

$$\Lambda = \frac{1}{8}\left(\frac{R}{\ell_D}\right)^2 = \frac{\ell_B R^2 \bar{c}}{\ell_B R^2 \bar{c} + 2}. \tag{7}$$

2.3 Proton flow

A channel with negatively charged walls is considered in this work. The channel is coupled to large electrolyte reservoirs at both openings. For a sufficiently large, negative surface charge density and narrow channels, it is warranted to neglect the presence of co-ions in the channel. This case corresponds to highly charged channels for which the Donnan relations point to a vanishing co-ion concentration [33]. For large aspect ratios, the double layers at the pore openings occupy only a small fraction of the entire channel length and the analysis can be restricted to the channel interior outside of these boundary regions. However, it should be kept in mind that the boundary conditions for fluid simulations of the channel interior are ultimately to be coupled to the conditions of the reservoirs through the Donnan equilibrium.

The transport of protons is governed by the Nernst–Planck equation. The total proton flux density, $\mathbf{j}$, includes contributions from advection, concentration gradients, and electrostatic potential gradients (i.e., the electric field),

$$\mathbf{j} = c\mathbf{v} - D\nabla c + \mu q c \mathbf{E}, \tag{8}$$

which enters the continuity equation for protons,

$$\frac{\partial c}{\partial t} + \nabla \cdot \mathbf{j} = 0. \tag{9}$$

In equation (8), D denotes the diffusion coefficient of protons, which is assumed independent of r, and $\mu = D/k_B T$ is the proton mobility. Using cross-sectional averaging, the 1-D version of the Nernst–Planck equation (8) for the axial direction was found to be [32]

$$\bar{j}_z = \bar{c}\bar{u}_z(1-\xi_u) + \frac{R^2 q \bar{c}^2 \bar{E}_z}{4\nu}(1-\xi_E) - D\left(\frac{\partial \bar{c}}{\partial z} - \ell_B R \bar{c}^2 \frac{\partial R}{\partial z}\right) + \mu q \bar{c} \bar{E}_z, \tag{10}$$

where ξ_E satisfies $0 \le \xi_E < 1$ and is a function of Λ,

$$\xi_E = \frac{1}{3}\Lambda + \frac{5}{36}\Lambda^2 + \frac{4}{45}\Lambda^3 + \mathcal{O}(\Lambda^4). \tag{11}$$

Again, ξ_E is related to the flow solutions found by Berg et al. [4] for the case of an infinite, straight channel with a circular cross-section.

2.4 Dimensionless fluxes

For easier handling of the otherwise complex formulations that follow, equations (5) and (10) are non-dimensionalized using properties of the initially equilibrated channel.

The following non-dimensionalization scheme is used,

$$x = \frac{z}{L_0},\ \tilde{R} = \frac{R}{R_0},\ \tilde{u} = \frac{\bar{u}_z}{\left(\frac{|\sigma_0|R_0\Delta V_0}{4\nu L_0}\right)}, \tag{12}$$

$$\tilde{p} = \frac{\bar{p}}{\left(\frac{2|\sigma_0|\Delta V_0}{R_0}\right)},\ \tilde{c} = \frac{\bar{c}}{\left(\frac{2|\sigma_0|}{qR_0}\right)},\ \tilde{E} = \frac{\bar{E}_z}{\left(\frac{\Delta V_0}{L_0}\right)}. \tag{13}$$

This gives the fluid and proton flux densities,

$$\tilde{u} = -\tilde{R}^2\left(\frac{\partial\tilde{p}}{\partial x} - \tilde{c}\tilde{E}[1-\xi_u]\right), \tag{14}$$

$$\tilde{j}_z = \tilde{c}\tilde{u}[1-\xi_u(\tilde{R})] - \mathcal{K}_{\text{diff}}\left(\frac{\partial\tilde{c}}{\partial x} - 2\kappa\tilde{R}\tilde{c}^2\frac{\partial\tilde{R}}{\partial x}\right) + \left(\mathcal{K}_{\text{migr}} + 2(\tilde{R}\tilde{c})^2(1-\xi_E)\right)\tilde{E}, \tag{15}$$

where $\mathcal{K}_{\text{diff}} = \frac{4\nu D}{|\sigma_0|R_0\Delta V_0}$ and $\mathcal{K}_{\text{migr}} = \frac{4\nu qD}{|\sigma_0|R_0 k_{\text{B}}T}$ measure the strengths of the diffusion and migration fluxes, respectively, relative to the convection flux from electroosmotic forces. ΔV_0 is a reference axial voltage drop. Finally, $\kappa = \ell_{\text{B}}|\sigma_0|R_0/2q$ is a new dimensionless parameter introduced so that $\Lambda = \frac{\kappa\tilde{R}^2\tilde{c}}{1+\kappa\tilde{R}^2\tilde{c}}$. Note that the overhead bar on symbols is used for cross-sectionally averaged variables, and the overhead tilde is used for dimensionless versions of those variables after normalization via (12) and (13).

The Kelvin-Voigt model that considers the balance of normal pressure forces on the walls due to the fluid pressure, electroosmotic pressure and linear elastic pressure, gives [32]

$$\tilde{p} = \mathcal{K}_Y\left(\frac{\tilde{R}-1}{\tilde{R}}\right) - \mathcal{K}_{\text{osm}}\tilde{c}(1+\kappa\tilde{R}^2\tilde{c}), \tag{16}$$

where $\mathcal{K}_Y = \frac{Yh_0}{2|\sigma_0|\Delta V_0}$ and $\mathcal{K}_{\text{osm}} = \frac{k_{\text{B}}T}{q\Delta V_0}$ measure the strength of elastic and osmotic forces, respectively, relative to electroosmotic forces.

3 Results and discussion

3.1 Onsager transport coefficients

In the linear response regime, the Onsager coefficient matrix $[\boldsymbol{\mu}]$ relates the volumetric water flux $Q = R^2\bar{u}_z$ and the axial proton current $I = qR^2\bar{j}_z$ to the pressure gradient $\nabla\bar{p} = \partial_z\bar{p}$ and the axial electric field $\bar{E}_z$ via

$$\begin{pmatrix} Q \\ I \end{pmatrix} = \begin{pmatrix} \mu_{\text{hyd}} & \mu_{\text{str}} \\ \mu_{\text{osm}} & \mu_{\text{ele}} \end{pmatrix}\begin{pmatrix} -\nabla\bar{p} \\ \bar{E}_z \end{pmatrix}. \tag{17}$$

The μ_{ij}'s denote Onsager phenomenological transport coefficients: $\tilde{\mu}_{\text{hyd}}$ characterizes the hydraulic conductance (and permeability) in accordance with Darcy's law, $\tilde{\mu}_{\text{ele}}$ the electric conductance in accordance with Ohm's law, $\tilde{\mu}_{\text{osm}}$ the electroosmotic effect, and $\tilde{\mu}_{\text{str}}$ the streaming potential effect.

We assume that in the system under consideration the fixed charges located on the walls are balanced by a proton concentration $\bar{c}$ inside the channel and in each cross-section so that global and local electroneutrality are both preserved. This condition is met for long-aspect-ratio channels, for which (i) the rate of change of the electric field in the axial direction is much slower than that in the radial direction and (ii) the radius varies gradually along the pore. From equation (2), this condition yields

$$\tilde{c} = \frac{1}{\tilde{R}^{1+\alpha}}. \tag{18}$$

Essentially, these assumptions eliminate any free choice in concentration gradients, leaving only two driving forces (due to gradients in pressure and electric potential) for two fluxes, those of water and ions. This consistent description would need to be extended to three driving forces, including concentration gradients, and three fluxes, including co-ions, if local electroneutrality is not guaranteed [33].

Using equations (14), (15), (16) and (18), and setting $\tilde{a} = \tilde{R}^2$, one finds the transport coefficients

$$\mu_{\mathrm{hyd}} = \left(\frac{R_0^4}{8\nu}\right)\tilde{a}^2, \tag{19}$$

$$\mu_{\mathrm{ele}} = \frac{(R_0\sigma_0)^2}{2\nu}\left\{\tilde{a}^{(1-\alpha)/2}\left[\mathcal{K}_{\mathrm{migr}} + 2\tilde{\tilde{a}}^{(1-\alpha)/2}[1-\xi_E(a)]\right] + \tilde{a}^{1-\alpha}[1-\xi_u(\tilde{a})]^2\right\}. \tag{20}$$

$$\mu_{\mathrm{str}} = \frac{R_0^3\sigma_0}{4\nu}\left\{\tilde{a}^{(3-\alpha)/2}\left[1-\xi_u(\tilde{a})\right]\right\}. \tag{21}$$

$$\mu_{\mathrm{osm}} = \begin{cases} \mu_{\mathrm{str}}, & \text{rigid channel.} \\ \mu_{\mathrm{str}} + \dfrac{R_0^3\sigma_0}{4\nu}\left\{\dfrac{\mathcal{K}_{\mathrm{diff}}\left[2\kappa\sqrt{\tilde{a}} + \tilde{a}^{\alpha/2}(1+\alpha)\right]\tilde{a}^{1-\alpha}}{\mathcal{K}_Y + \mathcal{K}_{\mathrm{osm}}\left[2\sqrt{\tilde{a}} + \tilde{a}^{\alpha/2}(1+\alpha)\right]}\right\}, & \text{deformed channel.} \end{cases} \tag{22}$$

From (22), Onsager's reciprocal relation is upheld with $\mu_{\mathrm{osm}} = \mu_{\mathrm{str}}$ when the channel has a uniform radius and is rigid ($\mathcal{K}_Y \to \infty$). However, when the channel is deformed and has non-uniform radius, the symmetry of $[\boldsymbol{\mu}]$ is broken. A channel curvature, or more precisely a gradient in the channel radius $\partial_z R$, introduces a diffusional proton-driving force. This results in a violation of Onsager's reciprocal relation. Since p is related to R according to (16), we do not classify $\partial_z R$ or $\partial_z A$, where A is the cross-sectional area of the channel ($\partial_z A = \partial_z[\pi R^2]$), as a thermodynamic force. After all, they can be expressed in terms of $\partial_z p$ which is a true driving force. Instead, we refer to $\partial_z A$ as a pseudo-force and it is associated with the curvature coefficient,

$$\mu_{\mathrm{curv}} = \frac{\sigma_0^2\Delta V_0}{2\nu}\left\{\frac{\mathcal{K}_{\mathrm{diff}}\left[2(\tilde{a}^{(1-\alpha)/2}\kappa + 1) - (1-\alpha)\right]\tilde{a}^{(1-\alpha)/2}}{2\tilde{a}}\right\}. \tag{23}$$

It stems from the reduction of a three-dimensional system to a one-dimensional problem, coupled with local electroneutrality. In contrast, in the original three-dimensional formulation of the problem, Onsager's reciprocal relations are not violated at any point in the fluid.

In the deformed state, the system's linear response can be formulated as

$$\bar{\mathbf{J}} = [\boldsymbol{\mu}]\bar{\mathbf{X}} + \bar{\boldsymbol{\xi}}, \tag{24}$$

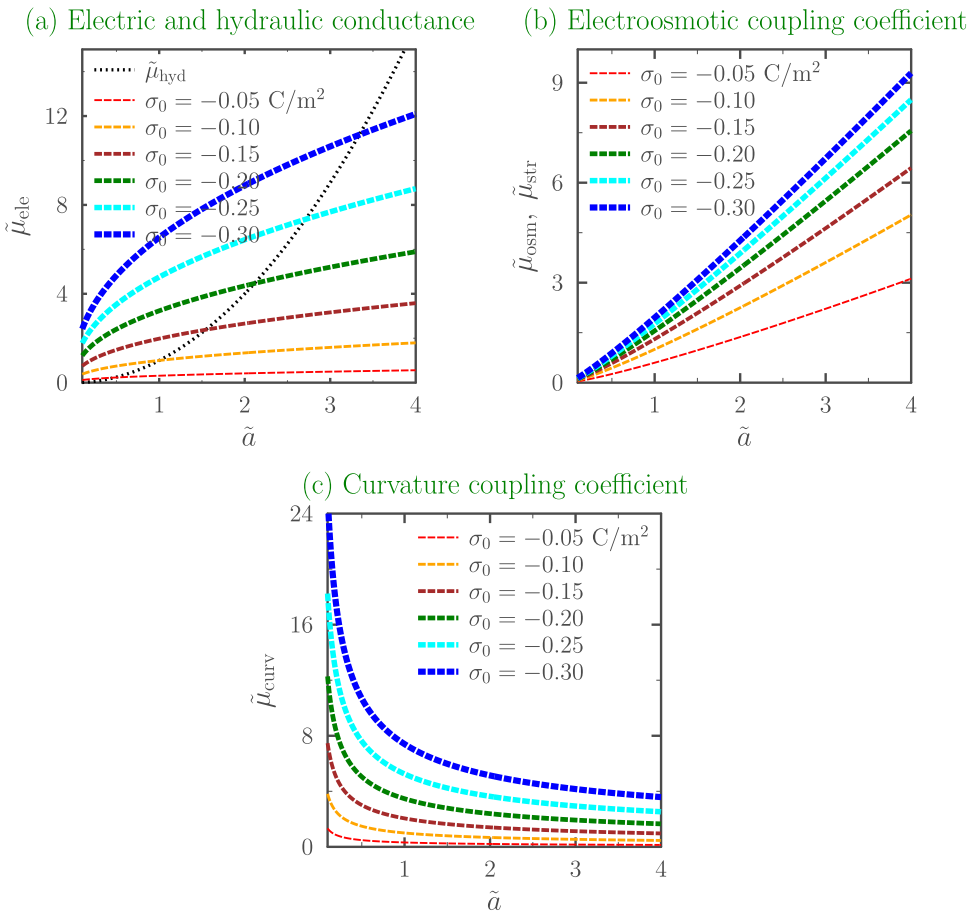

Fig. 2. Transport coefficients against the pore area $\tilde{a}$. Coefficients are normalized with reference parameters, i.e., $\tilde{\mu}_{\rm ele} = \mu_{\rm ele}/\left(\mu_{\rm ele}\right)_{\rm ref}$, etc. The fixed parameters used as reference are: $L_0 = 50\,\mu$m, $D = 7 \times 10^{-6}\,$cm^2/s, $\Delta V_0 = 0.1\,$V, $R_0 = 2\,$nm, $Y = 0.05\,$GPa, $T = 300\,$K, $h_0 = 1\,$nm, $\epsilon = 45$, $\nu = 3.35 \times 10^{-4}\,$Pa s, and $\alpha = 0.5$.

where $\bar{\mathbf{J}} = [Q,\ I]^T$, $\bar{\mathbf{X}} = [-\nabla p,\ E_z]^T$ and $\bar{\boldsymbol{\xi}} = [0,\ \mu_{\rm curv}\partial_z A]^T$ give the thermodynamic fluxes, thermodynamic forces and the diffusional pseudo-force, respectively.

Figure 2 shows plots of the transport coefficients as a function of the channel cross-sectional area relative to its equilibrium area (note that $\tilde{a} = A/A_{\rm eq}$), for different values of σ_0. Coefficients are normalized with reference parameters, i.e., $\tilde{\mu}_{\rm ele} = \mu_{\rm ele}/\left(\mu_{\rm ele}\right)_{\rm ref}$, etc. Figure 2a illustrates the relative strength of electric and hydraulic conductance at different values of $\tilde{a}$. The model predicts that electric conductance increases with σ_0 in a concave fashion. On the other hand, the hydraulic conductance, which is independent of σ_0, increases in a convex manner and eventually dominates electric conductance as the radius grows much larger than the relaxed state. Very large $\tilde{a}$ ramps up the fluid pressure within the channel, owing to the enhanced elastic response of the channel walls. This directly leads to high pressure-induced water flux, and hence large hydraulic conductance. Figure 2b shows the expected linear increase of electroosmotic and streaming coupling coefficients with $\tilde{a}$. The curvature coefficient, which measures the extent to which the system's Onsager symmetry is broken as a result of curvature-induced proton diffusion, is plotted in

Figure 2c. The symmetry breaking is more pronounced at small $\tilde{a}$ and large σ_0, equivalent to highly charged channels.

3.2 Electrokinetic energy conversion

In this part, we investigate the thermodynamic efficiency of (1) electrokinetic power harvesting devices and (2) electrokinetic pumping devices. Energy conversion is realized in an individual nanochannel by means of streaming currents, electric field, and the pressure-driven transport of protons in the EDL. The schematic for the case of power harvesting is illustrated in Figure 1. The resistance of the reservoirs is neglected in our calculations. In order to calculate the conversion efficiency, transport properties explored in Section 3.1 have to be determined.

The thermodynamic efficiency χ of energy conversion is defined as the ratio of useful power output, P_{out}, to power consumption, P_{in}:

$$\chi = \begin{cases} \dfrac{I\bar{E}_z}{Q\nabla\bar{p}}, & \text{electrical power generation mode.} \\ \dfrac{Q\nabla\bar{p}}{I\bar{E}_z}, & \text{pumping mode.} \end{cases} \tag{25}$$

Substituting Q and I with the expressions in (17), P_{out} and χ for each energy conversion mode in (25) are established as functions of the output thermodynamic force only, provided the input thermodynamic forces and all Onsager transport coefficients are known. Therefore, the output thermodynamic force and the conversion efficiency under maximization of either (1) the power output P_{out} or (2) the efficiency χ can be obtained separately.

3.2.1 Maximizing power output

We start by working out the output thermodynamic forces ($\bar{E}_{\max}$ for power generation mode and $\nabla\bar{p}_{\max}$ for pumping mode) and efficiency $\chi_{\max}$ at maximum power output ($I\bar{E}_z$ for power generation mode and $Q\nabla\bar{p}$ for pumping mode). This is done by differentiating P_{out} with respect to the corresponding output thermodynamic force. For the two conversion modes, one obtains the maximum output forces,

$$\bar{E}_{\max} = \frac{\mu_{\text{osm}}}{2\mu_{\text{ele}}}\nabla\bar{p}, \tag{26}$$

$$\nabla\bar{p}_{\max} = \frac{\mu_{\text{str}}}{2\mu_{\text{hyd}}}\bar{E}_z. \tag{27}$$

The efficiency at maximum power output, which is the same for both power generation and pumping modes, can be shown to be

$$\chi_{\text{maxP}} = \frac{\chi_0}{2}\,\frac{\beta}{(2-\beta)}, \tag{28}$$

where $\beta = (\mu_{\text{osm}}/\mu_{\text{ele}}) \times (\mu_{\text{str}}/\mu_{\text{hyd}})$ and $\chi_0 = \mu_{\text{osm}}/\mu_{\text{str}}$. The dimensionless parameter β is a cross-correlation coefficient, usually called the 'figure of merit' [34,35],

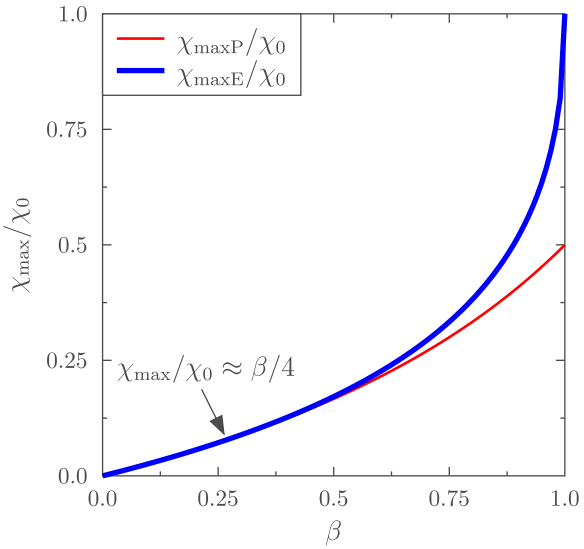

Fig. 3. Dependence of electrokinetic conversion efficiency on the cross-correlation coefficient at maximum output power and maximum efficiency.

and can be described as the product of the streaming current effect and the electro-osmotic effect. The coefficient χ_0 measures the symmetry of the Onsager coefficient matrix $[\boldsymbol{\mu}]$, and it assumes a value of 1 for rigid channels.

3.2.2 Maximizing efficiency

Using a similar approach, we determine the output forces that maximize the conversion efficiency. This is done by differentiating χ with respect to the corresponding output thermodynamic force. The resulting optimum output forces obtained for pumping and power generation modes, respectively, are

$$\bar{E}_{\max} = \frac{\mu_{\text{hyd}}}{\mu_{\text{str}}} \left(1 - \sqrt{1-\beta}\right) \nabla \bar{p}, \tag{29}$$

$$\nabla \bar{p}_{\max} = \frac{\mu_{\text{ele}}}{\mu_{\text{osm}}} \left(1 - \sqrt{1-\beta}\right) \bar{E}_z. \tag{30}$$

The corresponding efficiency, which is also the same for both power generation and pumping modes, can be shown to be

$$\chi_{\max E} = \chi_0 \left(\frac{1-\sqrt{1-\beta}}{1+\sqrt{1-\beta}}\right), \tag{31}$$

and all equations are valid under the constraint $0 \leq \beta < 1$ to maintain non-negative intrinsic entropy generation in electrokinetic flows. Variation of $\chi_{\max P}/\chi_0$ and $\chi_{\max E}/\chi_0$ with β is shown in Figure 3. In the low β limit (i.e., $\beta \to 0$), both $\chi_{\max P}/\chi_0$ and $\chi_{\max E}/\chi_0$ vary linearly with β ($\chi_{\max}/\chi_0 \approx \beta/4$). In the high β limit (i.e., $\beta \to 1$), $\chi_{\max P}/\chi_0$ and $\chi_{\max E}/\chi_0$ are monotonically increasing functions of β, with $\chi_{\max P}$ assuming half the value of $\chi_{\max E}$.

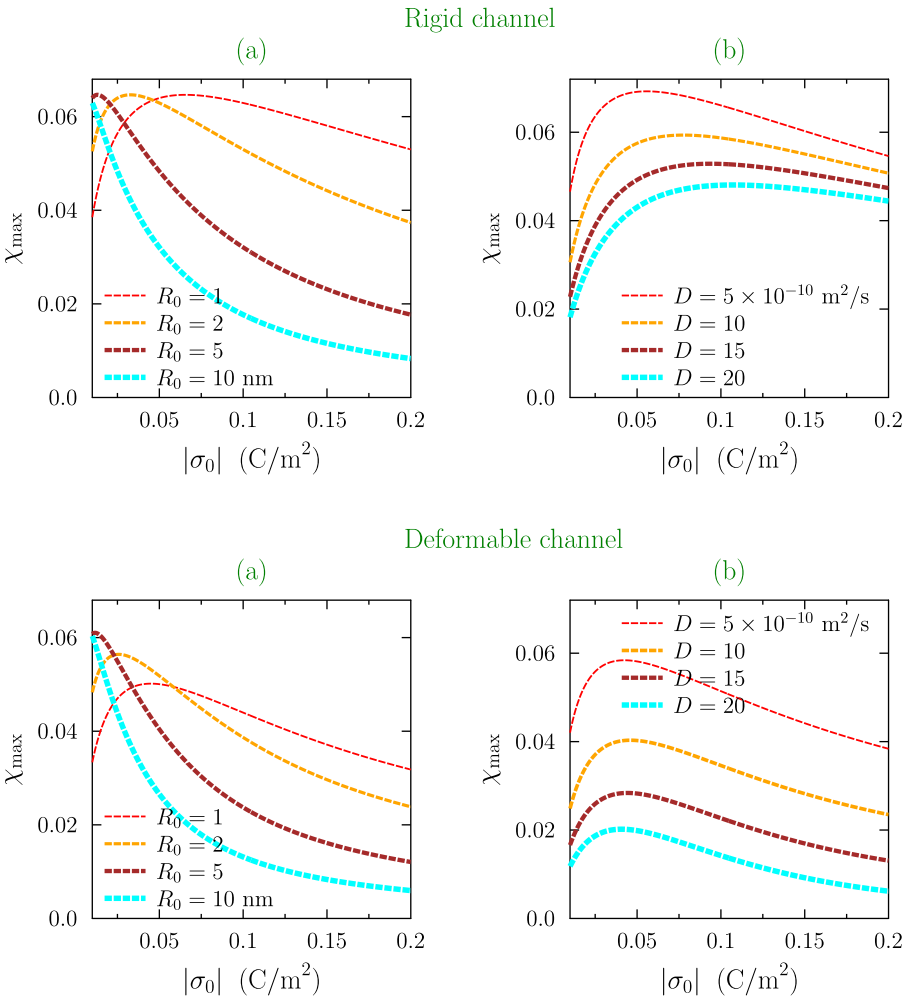

Fig. 4. Electrokinetic energy conversion efficiency at maximum efficiency against surface charge density at different (a) channel radii and (b) cation diffusion constants. The first row corresponds to the case of a rigid channel and the second row is for a deformable channel. Results are obtained via (31). Among the fixed parameters used as references are: $D = 7 \times 10^{-6}\,\mathrm{cm}^2/\mathrm{s}$, $R_0 = R = 2\,\mathrm{nm}$, $Y = 0.05\,\mathrm{GPa}$, $T = 300\,\mathrm{K}$, $h_0 = 1\,\mathrm{nm}$, $\epsilon = 45$, $\nu = 3.35 \times 10^{-4}\,\mathrm{Pa\,s}$, and $\alpha = 0.5$.

Plots of maximum efficiency determined via (31) against σ_0, which are almost the same as those obtained from (28) for the case of $\beta \ll 1$ (i.e., $\chi_{max} = \chi_{maxP} = \chi_{maxE}$), are shown in Figure 4. For a typical set of parameters, χ_{max} is on the order of 5%, and β is on the order of 0.2. The behaviour is similar to what has been reported from experiments [36–40]: χ_{max} increases with σ_0 for small σ_0 but reaches a maximum at an absolute value of around $0.05\,\mathrm{C/m}^2$; a further increase in σ_0 results in a decrease in χ_{max}. At very large σ_0, corresponding to regions past the peak, the coupled fluid-ion transport is reduced since a large fraction of protons occupy the EDL where fluid flow is significantly hampered. This affects both electroosmotic flow and the streaming current.

Furthermore, we explored the dependence of χ_{max} on R_0 and D for the case of a rigid channel, and then for a deformable channel using results from (31). For a

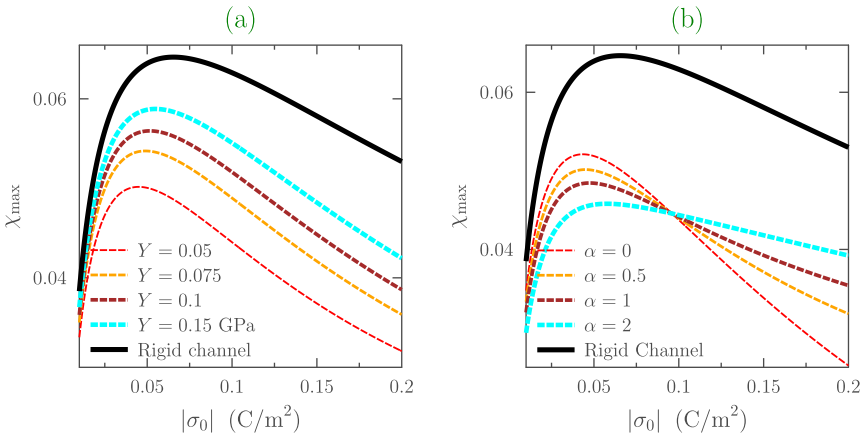

Fig. 5. Electrokinetic energy conversion efficiency at maximum efficiency against surface charge density at different (a) elasticity constants and (b) values of surface geometry parameter α. Results are obtained via (31). Among the fixed parameters used as references are: $D = 7 \times 10^{-6}\,\mathrm{cm}^2/\mathrm{s}$, $R_0 = R = 2\,\mathrm{nm}$, $Y = 0.05\,\mathrm{GPa}$, $T = 300\,\mathrm{K}$, $h_0 = 1\,\mathrm{nm}$, $\epsilon = 45$, $\nu = 3.35 \times 10^{-4}\,\mathrm{Pa\,s}$, and $\alpha = 0.5$.

rigid channel, increasing R_0 only shifts the peak of χ_{max} towards smaller σ_0; whereas for a deformable channel, this effect further changes the value of χ_{max} at the peak. For large σ_0, χ_{max} achieves larger values when R_0 is small. The opposite effect is observed for small σ_0. Conditions for which a smaller fraction of protons reside in the EDL yield a higher χ_{max}. In other words, χ_{max} is optimized when the double layers from opposite walls of the channel overlap. From Figure 4, we see that higher proton diffusivity tends to lower the efficiency. This effect is even more significant for the case of a deformable channel where the pore curvature induces a diffusional force that opposes the migration of protons, thereby reducing the overall transport.

Finally, the dependence of χ_{max} on elastic and geometric properties of the channel is shown in Figure 5. In each plot, the black solid curve represents a rigid channel. χ_{max} increases with the elastic coefficient, Y. Optimum χ_{max} is realized when the pore is rigid. Hence, the model predicts that a softness of channel walls is not favourable for energy harvesting. For soft channels, energy is lost due to elastic deformations taking place along the walls, thereby changing the flow dynamics and reducing χ_{max} as a consequence. Figure 5b shows that χ_{max} is also influenced by α. All curves converge at one specific value of σ_0, which is $\sim 0.1\,\mathrm{C/m}^2$ for the case shown in Figure 5b. Below this value, smaller values of α optimize χ_{max}. The opposite is seen for values of σ_0 above this convergence point. The convergence can be well understood from the mathematical nature of the model used. Dependence on α, for the case of $\tilde{a} = 1$ and a deformable channel, is only seen through μ_{osm} given in (22). This dependence vanishes when $2\kappa = \mathcal{K}_Y/\mathcal{K}_{osm} + 2$, and this gives the value of σ_0 at which all curves converge.

One universal feature of the results reported here is that the efficiency gets amplified and peaks over a narrow regime at low σ_0. The peak region is not much affected by the channel's elasticity. Figure 6 compares results with data obtained from experiments and MD simulations. In Figure 6a, we compare with experimental results reported by Xi et al. [37], where the efficiency χ is plotted against the sectionally-averaged counterion concentration ($\bar{c} = 2|\sigma_0|/qR_0$). Xi et al. studied single track-etched nanopores by measuring the streaming currents and conductance. Data reported is from two of their samples, corresponding to nanopores with inner radii 32 nm and 31 nm. We use $R_0 = 32\,\mathrm{nm}$ and $D = 20 \times 10^{-6}\,\mathrm{cm}^2/\mathrm{s}$ to calculate

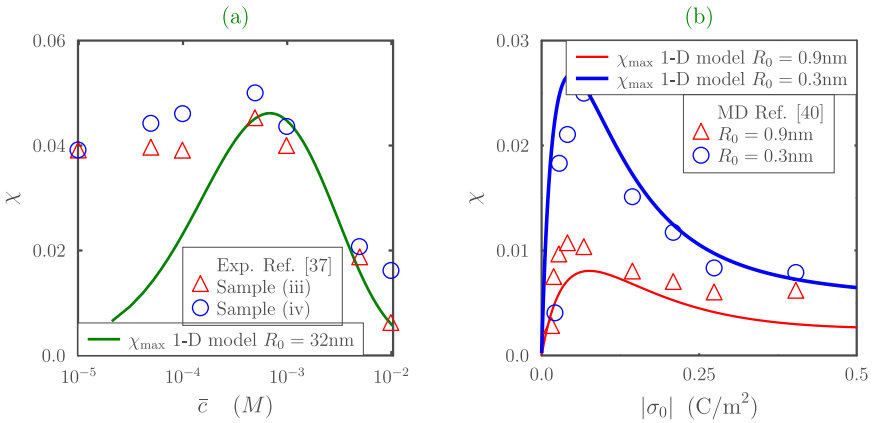

Fig. 6. Comparison of the 1-D model with (a) experimental results from reference [37] and (b) MD simulations results from reference [40]. For experimental results shown in (a), single track-etched nanopores with outer radius of 120 nm. Two samples are reported, with inner pore radii of 32 nm (sample (iii)) and 31 nm (sample (iv)). For MD simulations results shown in (b), pore radii of 0.3 nm and 0.9 nm were used and values of χ were scaled by a factor of 1/10 to make qualitative comparison. $D = 20 \times 10^{-6}$ cm^2/s was used for the model results in (a), and $D = 15 \times 10^{-6}$ cm^2/s was used in (b). Among the fixed parameters used are $Y = 0.5$ GPa, $T = 300$ K, $h_0 = 1$ nm, $\epsilon = 45$, $\nu = 3.35 \times 10^{-4}$ Pa s, and $\alpha = 0.5$.

$\chi_{\max}$ from the 1-D model and compare with the data. The peak region obtained in our 1-D model matches that from the experimental data. However, the model gives a larger decay of χ towards lower concentrations. This could arise from the track-etched feature of pores considered in reference [37]. In Figure 6b, we compare our 1-D model results with MD simulation results reported by Bakli and Chakraborty [40]. The numerical values they obtained for the efficiency are markedly higher than obtained in our model. This could be due to specific simulation conditions that are not well-captured by the model. Hence, we scaled their efficiency values by a factor of 1/10 to match our results. With this modification, we obtain the same qualitative behaviour as theirs. Data is from pores of radii 0.3 nm and 0.9 nm, and $D = 15 \times 10^{-6}$ cm^2/s was used for the model results. Our model gives an efficiency peak at a region that matches that from their data. Note that a deformable nanochannel ($Y = 0.5$ GPa and $\alpha = 0.5$) was assumed to obtain the 1-D model results in Figure 6.

4 Conclusions

This contribution employed continuum modelling to investigate the classical problem of electrokinetic transport in deformable nanochannels that are characterized by negative charges residing on the inner walls, balanced exactly by counter-ions in the fluid. Closed-form formulae for Onsager transport coefficients were derived first for the case of rigid and subsequently for deformable channels. For the general case of co- and counter-ions, the coefficients are only attainable numerically. For the limiting case of low co-ion concentration inside the channel, closed-form solutions may still be attainable via a perturbative analysis of the counter-ions-only case. Results reveal that the Onsager reciprocity principle holds for rigid channels but is not fulfilled when the channel is deformed. As demonstrated in this article, the symmetry violation is

caused by a "fictitious" contribution to diffusion introduced by the reduction of the model to 1D.

Furthermore, this work explored the energy conversion mechanism of electrokinetic systems. The maximum efficiency was calculated as a function of the phenomenological transport coefficients. We found that the efficiency of an electrokinetic system is maximized under conditions of strong double layer overlap within the channel. Moreover, the proposed model predicts that a softness of channel walls diminishes the efficiency compared to the rigid case.

References

1. H.L.F. Helmholtz, Wied. Ann. **7**, 337 (1879)
2. M. Smoluchowski, Phys. Z. **6**, 529 (1905)
3. P. Berg, K. Ladipo, Proc. R. Soc. A **465**, 2663 (2009)
4. P. Berg, J. Findlay, Proc. R. Soc. A **467**, 3157 (2011)
5. K.O. Ladipo, P. Berg, S. Kimmerle, A. Novruzi, Int. J. Chem. Phys. **134**, 074103 (2011)
6. A.J. Bard, L.R. Faulkner, *Electrochemical methods: fundamentals and applications*, 2nd edn. (Wiley, New York, 1980)
7. M.Z. Bazant, K. Thornton, A. Ajdari, Phys. Rev. E **70**, 021506 (2004)
8. S. Prakash, A.T. Conlisk, Lab Chip **16**, 3855 (2016)
9. S. Chung, O.S. Anderson, S. Olaf, V.V. Krishnamurthy, *Biological membrane ion channels: dynamics, structure, and applications* (Springer Science & Business Media, 2007)
10. S.J. Kim, S.H. Ko, K.H. Kang, H. Kwan, J. Han, Nat. Nanotechnol. **5**, 297 (2010)
11. M. Eikerling, A. Kulikovsky, *Polymer Electrolyte Fuel Cells: Physical Principles of Materials and Operation* (CRC Press, 2014)
12. H. Daiguji, P. Yang, A.J. Szeri, A. Majumdar, Nano Lett. **4**, 2315 (2004)
13. L. Onsager, Phys. Rev. **37**, 405 (1931)
14. L. Onsager, Phys. Rev. **38**, 2265 (1931)
15. B.J. Kirby, *Micro- and nanoscale fluid mechanics: transport in microfluidic devices* (Cambridge University Press, 2010)
16. F.F. Reuss, Mem. Soc. Imp. Natur. Moscou. **2**, 327 (1809)
17. G. Quincke, Pogg. Ann. Phys. **107**, 1 (1859)
18. K. Kreuer, S.J. Paddison, E. Spohr, M. Schuster, Chem. Rev. **104**, 4637 (2004)
19. M. Eikerling, A.A. Kornyshev, E. Spohr, Adv. Polym. Sci. **215**, 15 (2008)
20. S.G. Rinaldo, C.W. Monroe, T. Romero, W. Mérida, M. Eikerling, Electrochem. Commun. **33**, 5 (2011)
21. M. Eikerling, P. Berg, Soft Matter **7**, 5976 (2011)
22. M. Safiollah, P.A. Melchy, P. Berg, M. Eikerling, J. Phys. Chem. B **119**, 8165 (2015)
23. A.Z. Weber, J. Newman, Chem. Rev. **104**, 4679 (2004)
24. M. Eikerling, A. Kulikovsky, *Polymer Electrolyte Fuel Cells: Physical Principles of Materials and Operation* (CRC Press, 2014)
25. A. Kusoglu, M.H. Santare, M.A. Karlsson, J. Polym. Sci. Part B: Polym. Phys. **49**, 1506 (2011)
26. P.-E.A. Melchy, M.H. Eikerling, J. Phys.: Condens. Matter **27**, 325103 (2015)
27. K. Oguro, N. Fujiwara, K. Asaka, K. Onishi, S. Sewa, Electr. Polym. Actuat. Dev. **3669**, 64 (1999)
28. N. Fujiwara, K. Asaka, Y. Nishimura, K. Oguro, E. Torikai, Chem. Mater. **12**, 1750 (1999)
29. A.J. Duncan, D.J. Leo, T.E. Long, Macromolecules **41**, 7765 (2008)
30. Z. Peng, A. Morin, P. Huguet, P. Schott, J. Pauchet, J. Phys. Chem. B **115**, 12835 (2011)
31. J.B. Benziger, M.J. Cheah, V. Klika, M. Pavelka, J. Polym. Sci. Part B: Polym. Phys. **53**, 1580 (2015)
32. M. Matse, P. Berg, M. Eikerling, Phys. Rev. E **98**, 053101 (2018)
33. P.B. Peters, R. van Roij, M.Z. Bazant, P.M. Biesheuvel, Phys. Rev. E **93**, 053108 (2016)

34. F.A. Morrison Jr., J.F. Osterle, J. Chem. Phys. **43**, 2111 (1965)
35. Y. Zhang, Y. He, M. Tsutsui, X.S. Miao, M. Taniguchi, Sci. Rep. **7**, 46661 (2017)
36. J. Yang, F. Lu, L.W. Kostiuk, D.Y. Kwok, J. Micromech. Microeng. **13**, 963 (2003)
37. Y. Xie, X. Wang, J. Jin, K. Chen, Y. Wang, Appl. Phys. Lett. **93**, 163116 (2008)
38. C.C. Chang, R.J. Yang, Microfluid. Nanofluid. **9**, 225 (2010)
39. Y. Yan, Q. Sheng, C. Wang, J. Xue, H.C. Chang, J. Phys. Chem. C **117**, 8050 (2013)
40. C. Bakli, S. Chakraborty, Electrophoresis **36**, 675 (2015)